

# Satellite-Based Characterization of Convective Growth and Glaciation and Its Relationship to Precipitation Formation over Central Europe

FABIAN SENF AND HARTWIG DENEKE

*Leibniz Institute for Tropospheric Research, Leipzig, Germany*

(Manuscript received 29 August 2016, in final form 6 April 2017)


## ABSTRACT

The growth phase of convective storms and their transition to maturity is investigated based on more than 100 cases selected from the years 2012–14 over central Europe. Dynamical growth properties as well as cloud-top glaciation and microphysical characteristics are derived from the SEVIRI imaging radiometer aboard the geostationary Meteosat satellites. In addition, onset and intensity of surface precipitation are related to growth and glaciation processes using observations from the radar network of the German Weather Service. The majority of analyzed cases shows a distinct maximum in cloud-top cooling rate, which is used here for temporal synchronization. Cloud growth spans a period of approximately half an hour. Glaciation rate indicators suggest that freezing 15 min prior to the maximum cooling plays an important role in invigorating convective updrafts through the release of latent heat. Smaller ice particles are found for larger cloud-top cooling, which provides observational evidence that ice particles form later and have less time to grow in stronger convective updrafts. Furthermore, maximum cloud-top height, anvil expansion rate, maximum precipitation intensity, and core size are found to be positively correlated. With respect to the onset of precipitation, this analysis shows a high probability that significant precipitation already occurs 30 min prior to maximum cloud-top cooling.

## 1. Introduction

The limited understanding of dynamical and microphysical processes in deep convective clouds and their observable signatures poses a significant challenge for weather and climate research. One particular aspect concerns the application of our current knowledge of convective growth to the detection and short-term prediction of developing deep moist convection based on observational networks within the context of nowcasting (Wilson et al. 1998). Current observational systems approach their limits for rapidly developing deep convective clouds with temporal scales of tens of minutes and spatial scales on the order of 1 km or even less. To supplement radar measurements, cloud observations based on geostationary satellites have been proposed as important predictors of early detection of convective initiation (CI; Roberts and Rutledge 2003; Mecikalski

and Bedka 2006; Zinner et al. 2008; Mecikalski et al. 2010a,b; Siewert et al. 2010; Sieglaff et al. 2011; Merk and Zinner 2013; Sieglaff et al. 2014). Several of the above-mentioned studies have shown that detailed knowledge about the growth phase of developing storms can be utilized to increase the predictive skill of nowcasting applications. Temporal changes in satellite-observed thermal radiation can indicate the rapid speed of cloud-top cooling (CTC) and therefore vertical ascent of cloud tops. For example, satellite-based CTC rates have been calculated by Roberts and Rutledge (2003) to quantify the growth of convective clouds induced by boundary layer convergence in the United States. It has been found that satellite-derived cloud growth rates potentially provide precursor information up to 30 min before radar-derived storm initiation. In addition, Mecikalski and Bedka (2006), Mecikalski et al. (2008), and Walker et al. (2012) have combined multispectral estimates of cloud depth, growth, and glaciation to assess the potential of convective storm development. Based on their CI scheme, average nowcast lead times of 30 min for early detection of convective events were achieved. An additional important parameter that is related to cloud growth and is readily detectable from

 Denotes content that is immediately available upon publication as open access.

Corresponding author: Fabian Senf, senf@tropos.de

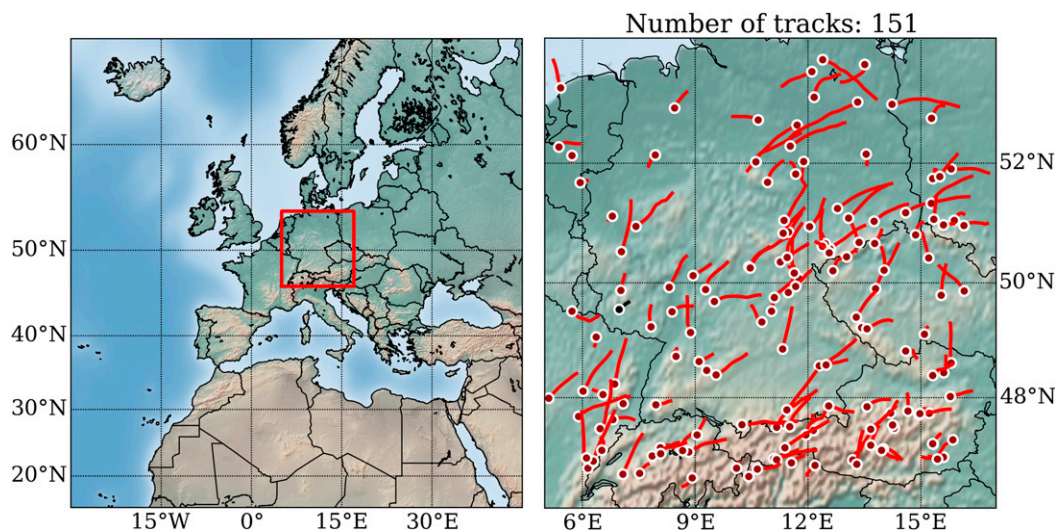


FIG. 1. (left) Overview of the domain of interest, which is marked by a red box, and (right) a collection of satellite-based storm tracks for all investigated cases. The tracks are plotted by red lines, and red circles with white edges highlight the track starting position. The black circle and line marks the case shown in Fig. 2.

geostationary satellites is the anvil area expansion rate. For instance, Machado et al. (1998) and Machado and Laurent (2004) have shown that the initial areal expansion of convectively forced anvils is proportional to the life times of mesoscale convective systems over the Amazon region. They have also demonstrated that, on average, the maximum area expansion occurs close to the time of maximum precipitation intensity. There is a long record of investigations connecting satellite-based cloud-top features with storm severity [e.g., Adler and Fenn (1979a,b), Reynolds (1980), and Heymsfield et al. (1983), among many others]. In essence, very cold cloud-top temperatures in the convective cores and several cloud-top morphological features as well as enhanced growth rates in terms of CTC and anvil expansion rate have been identified as discriminating factors for storm severity.

In the current study, we investigate convective cloud-top characteristics of growing storms over central Europe using geostationary satellite observations. We aim to provide relationships between cloud depth, growth, and glaciation properties and characterize the timing of formation of radar-derived moderate to heavy precipitation with regard to satellite-based growth and glaciation measures. We further discuss the relevance of our analysis within the context of satellite-based CI nowcasting. Our current approach is an extension of an earlier study (Senf et al. 2015) that was concerned with the characterization of initiation and growth of a few selected severe storms over central Europe. We are now able to confirm the significance of earlier results about the interrelationship between CTC and anvil macro- and microphysical changes. Furthermore, we supplement the investigation of

cloud dynamical characteristics by a joint analysis of multispectral glaciation rate estimates and their relationship to radar-derived precipitation formation. The paper is structured as follows: In section 2, we introduce the satellite and radar data. Storm tracking and the collection of along-track characteristics are explained in section 3. In section 4, we present the results of our study, which is concerned with the temporal behavior of indicators of cloud depth, growth, glaciation, and anvil and precipitation formation as well as interrelationships between the different variables. We finally give a summary and draw conclusions from our study in section 5.

## 2. Data

### a. Satellite data

We analyze data from the Spinning Enhanced Visible and Infrared Imager (SEVIRI), which is an optical imaging radiometer aboard the geostationary Meteosat Second Generation (MSG) satellites operated by the European Organisation for the Exploitation of Meteorological Satellites (EUMETSAT; Schmetz et al. 2002). So-called rapid-scan observations with a repeat cycle of 5 min have been chosen for the summer half-year periods, that is, from April to September, between 2012 and 2014. The operational rapid-scanning satellite, which was *Meteosat-8* until 9 April 2013 and was followed by *Meteosat-9*, is located at 9.5° E longitude and 0° N latitude. In the center of the domain of interest shown in Fig. 1, the infrared image pixel size is 3.2 km in the eastward direction and 6.1 km in the northward

direction. Within the whole marked region the pixel area varies from about  $17 \text{ km}^2$  in the south to  $22 \text{ km}^2$  in the north because of an increased viewing angle. The actual scan time of the rapid scan in the center of our domain is about 3 min, 30 s later than the nominal scan starting time.

SEVIRI is a multispectral instrument with 12 channels in the visible and infrared [see [Schmetz et al. \(2002\)](#) for further detail]. We use the high-resolution visible (HRV) channel, which has a threefold higher resolution than the narrow-band channels, and the window channel at  $10.8 \mu\text{m}$  for tracking of the convective cells. The radiation at  $10.8 \mu\text{m}$  is rather unaffected by absorption of atmospheric gases. Therefore, the  $10.8\text{-}\mu\text{m}$  brightness temperature (BT), denoted by  $T_{10.8}$ , can be used as proxy of the cloud-top temperature for optically thick clouds with optical thicknesses typically larger than 23 ([Rossow and Schiffer 1999](#)). Different time trends of  $T_{10.8}$  are calculated to characterize convective strength in terms of CTC during the growth phase and anvil expansion later on (see [section 3](#)). In addition, we study the behavior of several BT combinations, for example, the differences  $T_{8.7} - T_{10.8}$  and  $T_{10.8} - T_{12.0}$ , which carry information about the cloud-top particle phase, size, and shape [see [Matthee and Mecikalski \(2013\)](#) and references therein] and are taken to characterize the glaciation process of the cloud top. Further glaciation indicators are differences in the solar reflectances at  $0.6$  and  $1.6 \mu\text{m}$  ( $\rho_{0.6} - \rho_{1.6}$ ) and the reflected solar part of radiation at  $3.9 \mu\text{m}$  ( $\rho_{3.9}$ ), which is calculated after [Lindsey et al. \(2006\)](#) here. In the near-infrared, ice is more absorbing than liquid water, leading to a reduction of reflected solar radiation.

### b. Satellite products

A set of cloud products, including cloud mask, cloud type, and cloud-top height (CTH), has been generated using EUMETSAT's Satellite Application Facility on support to Nowcasting and Very Short-Range Forecasting (NWCSAF) software package for the set of selected cases. The masking of the along-track fields is performed on the basis of the NWCSAF cloud mask and type product ([Derrien and Le Gléau 2005](#)). We examine the discrimination between cloudy and clear-sky pixels, but allow for cloud contaminated or partially cloudy pixels. Furthermore, semitransparent cirrus is identified based on the cloud type classification and is excluded from further analysis. The retrieval of properties of growing cumulus underneath cirrus clouds is challenging, and an in-depth discussion of this topic can be found in [Mecikalski et al. \(2013b\)](#). NWCSAF cloud-top height, which is calculated using temperature profiles obtained from ECMWF forecasts, and cloud-top ascent rates from corresponding height time trends are derived for investigation of convective development.

We use the Royal Netherlands Meteorological Institute [Koninklijk Nederlands Meteorologisch Instituut (KNMI)] cloud physical properties (CPP) retrieval (see [Roebeling et al. 2006](#); [Meirink et al. 2010](#)) to derive the cloud-top thermodynamic phase, cloud optical thickness, and the cloud-top effective particle radius  $R_{\text{eff}}$ . The algorithm follows the methodology of [Nakajima and King \(1990\)](#) and compares a simulated reflectance pair ( $\rho_{0.6}, \rho_{1.6}$ ) with the observation. The reflectance  $\rho_{0.6}$  in the visible range at  $0.6 \mu\text{m}$  is mainly related to the optical thickness; the other reflectance  $\rho_{1.6}$  in the near infrared at  $1.6 \mu\text{m}$  is affected by particle absorption and thus also sensitive to particle size, shape, and thermodynamic phase ([Baum et al. 2000](#)). The algorithm uses two distinct precalculated lookup tables for water droplets and for imperfect hexagonal ice crystals, respectively. Cloud optical properties are retrieved by iteratively minimizing the difference between observed and simulated reflectance pair ( $\rho_{0.6}, \rho_{1.6}$ ). The retrieval is limited to situations with sun zenith angles lower than  $75^\circ$ . In ambiguous situations, phase "ice" is assigned to pixels with cloud-top temperature lower than  $265 \text{ K}$  ([Wolters et al. 2010](#)).

The cloud-top effective radius and visible optical thickness can exhibit large variations and uncertainties ([Marshall et al. 2006](#); [Wolters et al. 2010](#)). Product uncertainties are caused by deviations from the retrieval assumptions, which include homogeneous cloud-top properties and thereby, for example, neglect 3D radiative effects. The complex morphology of convective cloud clusters leads to illuminated cloud sides, shaded cloud regions behind convective towers and, furthermore, partly cloud-filled pixels at cloud edges. A high degree of subpixel variability thus decreases the accuracy of cloud products. The high-resolution information contained in the HRV reflectances can be extracted to downscale information in SEVIRI's low-resolution channels (see, e.g., [Deneke and Roebeling 2010](#); [Mecikalski et al. 2013a](#)) or to construct high-resolution cloud products ([Bley and Deneke 2013](#)). However, these promising approaches have not been applied in the current study and are left for future investigations. We hence emphasize that the retrieved cloud microphysical properties should be interpreted carefully. The reader should keep in mind that the products always refer to a hypothetical microphysical state of an idealized, horizontally homogeneous prototype cloud with similar radiative signatures to the observation, and does not necessarily match the actual convective cloud properties because of violations of the retrieval assumptions.

### c. Precipitation radar data

The radar reflectivity factor  $Z$  is used as a simple proxy of precipitation intensity in this study. The value of  $Z$  is

obtained from the German Radolan RX composite, in which radar data from a Germany-wide network of 16 C-band Doppler radar stations are merged into one homogenized and regularly gridded product (see, e.g., Wapler et al. 2015). The RX composite only uses data from precipitation scans that are performed at the lowest elevation following the apparent horizon. No attenuation correction is applied. The data are available every 5 min, and the scan is finished in less than 1 min after the nominal scan time. The spatial resolution is 1 km in both grid directions. Depending on the surrounding landscape and the distance between the radar antenna and the scattering target, the signal can be reflected up to 2 to 3 km above ground level. However, because of the merging strategy in regions of overlapping radars, accurate scan height information is not always available. No further quality assessments or corrections have been applied to the radar data in this study.

### 3. Method

#### a. Satellite-based tracking and calculation of along-track properties

The satellite-based tracks of storm cells are constructed in a semiautomated fashion, which is described in detail in appendix A. In essence, convective anvils are tracked automatically forward in time relying on the overlap of cells in successive satellite images, whereas growing cumulus clouds are manually tracked backward in time during the early development stage. A set of more than 100 satellite-based tracks has been chosen for the analysis that were randomly sampled from the summer half-year periods between 2012 and 2014 to limit the effort for manual tracking. These tracks and their initial starting location are shown in Fig. 1.

Along-track properties and 5-min time rates are calculated for several satellite-based proxies of cloud depth, growth, and glaciation. Uncertainties of along-track properties that are mainly caused by limitations in the spatial resolution of the satellite sensor are estimated from a  $3 \times 3$  region centered around the track. One particular time rate that has special importance for our study is the negative time trend of  $T_{10.8}$ , often referred to as the CTC rate. Median CTC rates represent cooling trends of all ascending cloud tops over a spatial domain of 120–150 km<sup>2</sup>.

The time of maximum CTC ( $t_{\text{cool}}$ ) is taken for synchronization of all considered properties and rates. It marks a common stage for growing convective cells, which divides the growth phase into an early intensification period before, and a continued growth period after the maximum of CTC (Senf et al. 2015).

The synchronization is performed on median and interquartile-range sequences by linearly interpolating the variables onto a common regular relative time coordinate  $t_{\text{rel}} = t - t_{\text{cool}}$ , similar to the approach used in Mecikalski et al. (2016).

#### b. Anvil and precipitation area calculations

The methodology of anvil detection and characterization closely follows the method applied by Senf et al. (2015). The anvil area is determined by 4-connectivity clustering, which assigns the connected area of the  $T_{10.8}$  field below 240 K to one cell. An equivalent diameter is calculated from the anvil area, which is the diameter of an equal-area circle. The temporal change of the corresponding equivalent radius approximates the average outward-pointing velocity  $u_r$  of the anvil edge, which is termed anvil edge velocity in the following. By definition,  $u_r$  is defined relative to the storm motion. The methodology is unable to capture the growth period of secondary storm cells initiating in the vicinity of primary cells, and thus gives preference to isolated convective development.

Precipitation data are also collected along satellite-based tracks. After parallax correction, a combination of automatic clustering and manual selection was applied to derive radar objects that are causally related to the satellite-derived cloud information (see appendix A for details). Each radar object is composed of a set of Z values above 35 dBZ that are not necessarily connected. This reflectivity threshold agrees with the typical threshold used for the definition of CI [see, e.g., Roberts and Rutledge (2003) and Mecikalski and Bedka (2006), among many others]. Using a standard Z–R relationship, it corresponds to a rainfall rate of 6 mm h<sup>−1</sup>. Please note that it is a common situation, at least for our set of cases, that developing convective cells observable at the resolution of the satellite observations are associated with multiple precipitation cores resolved by the radar composite.

In a further analysis step, two different thresholds at 46 and 55 dBZ are applied separately to each radar object. Cell area, diameter, and expansion rate are calculated for the parts of the Z field above the respective threshold. For simplicity, we only calculate diameters and radius rates of equal-area circles even for very complex-shaped precipitation clusters, and do not consider shape or other morphological properties in the analysis. The threshold of 46 dBZ is used in the German Weather Service nowcasting tool Konvektionsentwicklung in Radarprodukten (convection evolution in radar products) (KONRAD) [see, e.g., Wapler and James (2015) and references therein]. It is typically related to heavy rain of 35 mm h<sup>−1</sup> or more. The largest threshold of 55 dBZ is considered



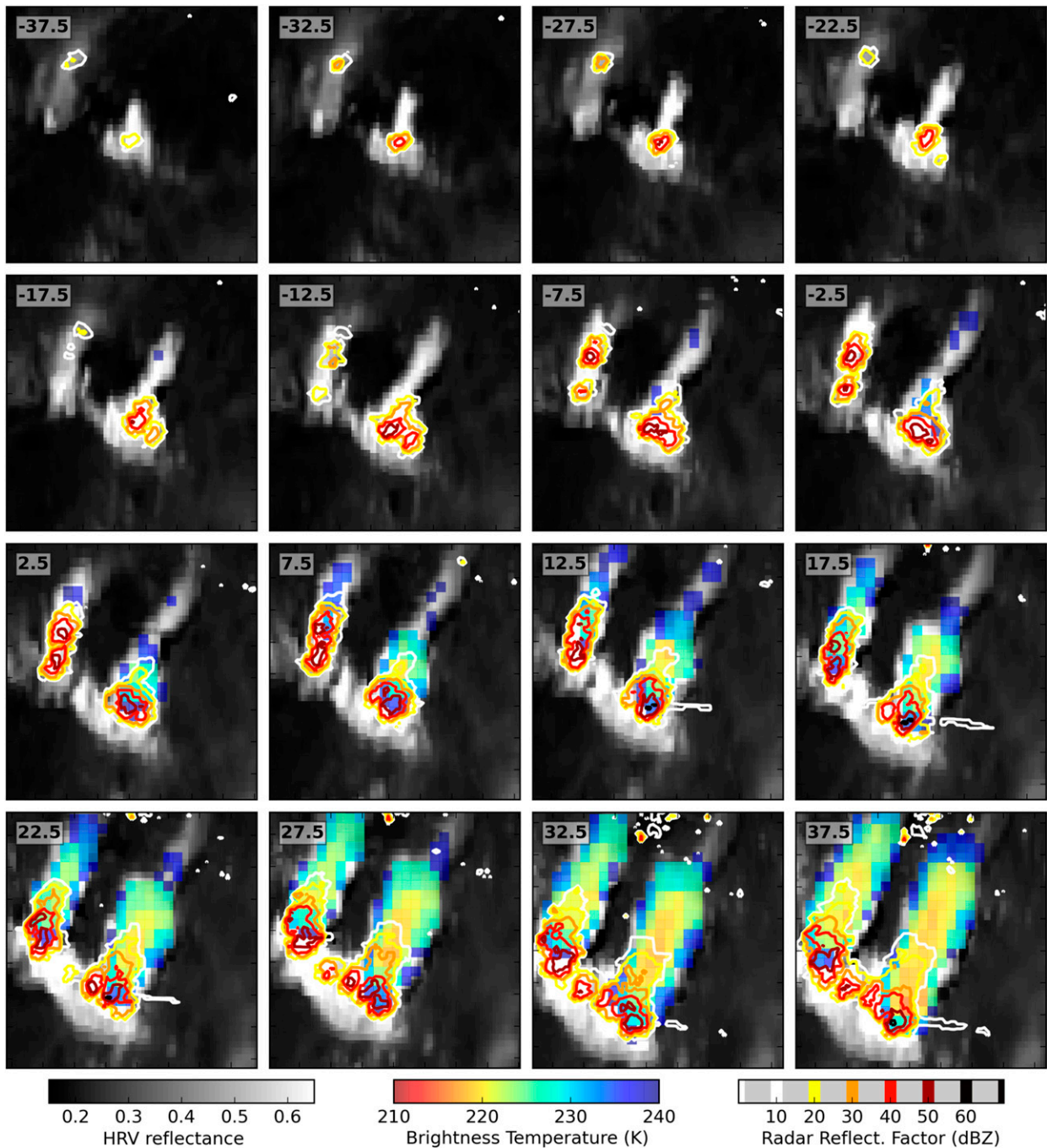


FIG. 2. Sequential convective development of a convective storm that initiated at 51.666°N, 10.920°E and 0945 UTC 27 Jul 2014. The numbers in the upper-left boxes indicate the nominal scan time relative to the CTC maximum in minutes. The HRV reflectance  $\rho_{\text{HRV}}$  is shown by the gray shadings, the 10.8- $\mu\text{m}$  brightness temperature masked for  $T_{10.8} > 240$  K is given in color shadings, and the radar reflectivity is plotted with contours (see section 2 for definition of variables). The individual cutouts are centered around the parallax-corrected track position and have a size of  $\pm 40$  km in the two directions. Terms  $\rho_{\text{HRV}}$  and  $T_{10.8}$  have been resampled and parallax corrected for plotting.

as first indicator for hail, and is used for issuing hail warnings at the German Weather Service. In a last step, the precipitation cell properties have also been synchronized to  $t_{\text{cool}}$ , taking into account the time shift due

to the difference in scan times of satellite and radar measurements.

Figure 2 shows a representative example of a developing convective cell characterized by the combined

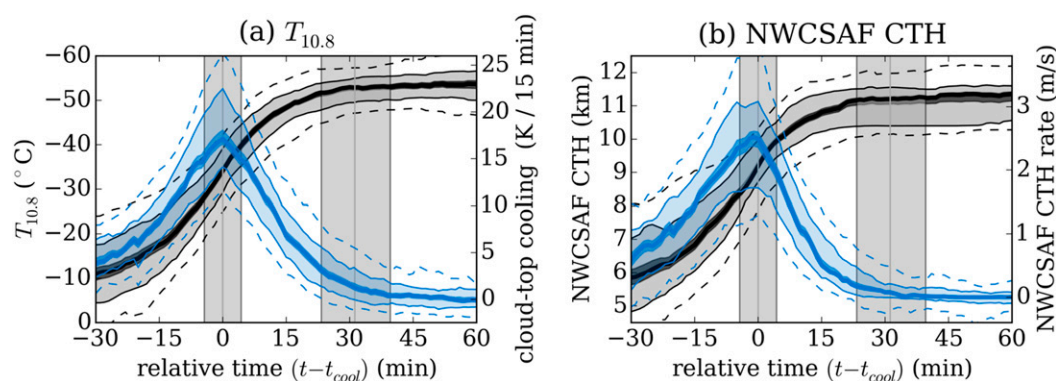


FIG. 3. Temporal behavior of (a)  $T_{10.8}$  and (b) NWCSAF CTH as function of relative time  $t_{\text{rel}} = t - t_{\text{cool}}$  (see section 2). Blue curves show the 5-min time trends of the respective variables. Median (thick solid line), interquartile range (light shaded interval with thin solid lines), and 10th and 90th percentiles (upper and lower dashed lines) are calculated from the set of more than 100 storm cases. Dark shaded intervals around the median (mainly visible for the time rates) give 2 times the interquartile range divided by the square root of the number of involved cases, which varies as a function of  $t_{\text{rel}}$ . This interval can be interpreted as confidence interval. In addition, the time of maximum CTC and maturation time as well as its uncertainty range is shown by gray vertical lines and shaded intervals, respectively.

use of satellite and radar data. Prior to the deep convective development, a convective cloud field is noticeable from the HRV reflectances. Precipitation develops around 30 min before the maximum CTC. The later anvil development is evident in the 10.8- $\mu\text{m}$  BTs.

## 4. Results

### a. Cloud depth and growth indicators

Figure 3 shows indicators of cloud-top height and vertical extent for the set of developing convective storms synchronized to the relative time  $t_{\text{rel}} = t - t_{\text{cool}}$ . On average,  $T_{10.8}$  values lie around  $-11^{\circ}\text{C}$  at 30 min before  $t_{\text{cool}}$ , decrease down to  $-33^{\circ}\text{C}$  at maximum cooling, and finally reach a steady state value at around  $-53^{\circ}\text{C}$  about 30 min after  $t_{\text{cool}}$  (Fig. 3a). The spread of  $T_{10.8}$  curves significantly decreases from  $10^{\circ}\text{C}$  at  $t_{\text{rel}} = -30$  min down to  $5^{\circ}\text{C}$  at  $t_{\text{rel}} = 30$  min. This is likely caused by the larger variability in environmental boundary layer and CI conditions relative to variations in the cloud equilibrium level. In addition, the temporal evolution of cloud-top height above sea level is given in Fig. 3b. Median values are around 6, 9, and 11 km for  $t_{\text{rel}} = -30, 0,$  and 30 min, respectively.

The CTC rates (Fig. 3a) and cloud-top vertical ascent rates (Fig. 3b) show a characteristic peak around the time of maximum CTC. This is essentially due to the synchronization strategy and therefore not unexpected, but is, however, an encouraging confirmation of this strategy. The maximum CTC rates, which are calculated as negative 5-min time trends of  $T_{10.8}$ , range

between  $14^{\circ}$  and  $22^{\circ}\text{C}$  per 15 min for 50% of our cases. This corresponds to cloud-top ascent rates between 1.7 and  $3\text{ m s}^{-1}$ , which are calculated as 5-min time trends of the NWCSAF cloud-top-height product. The growth duration—that is, the time period between half the value of the CTC maximum—is around 30 min, whereas the significant cooling signal that defines the overall growth phase lasts around 1 h. These values compare well to the CTC rates reported in Adler and Fenn (1979b) and Sieglaff et al. (2011, 2014), even though there exist some intrinsic differences in satellite sensor resolution, analysis techniques, and averaging strategies between these studies. Please note that the values of CTC rate reported by us in an earlier study are based on a very small set of cases are slightly smaller than the values reported here (Senf et al. 2015).

We also analyzed the temporal evolution of optical thickness and the BT difference  $T_{6.2} - T_{10.8}$  (not shown). The optical thickness shows a more constant and linear increase during the considered time period but is less certain than the infrared-based properties. Typical values lie around 20 at  $t_{\text{rel}} = -30$  min. The optical thickness increases to 40 at time of maximum CTC and reaches values close to 55 at 30 min thereafter. At  $t_{\text{rel}} = -30$  min,  $T_{6.2} - T_{10.8}$  is strongly negative, with values around  $-30^{\circ}\text{C}$ , because of water vapor absorption/emission at higher altitudes, that is, lower temperatures, in comparison with the cloud-top temperature. In the temporal progression,  $T_{6.2} - T_{10.8}$  increases and reaches steady state values around  $0^{\circ}\text{C}$ , when the apparent emission in the two infrared channels comes from similar altitudes close to the tropopause level.

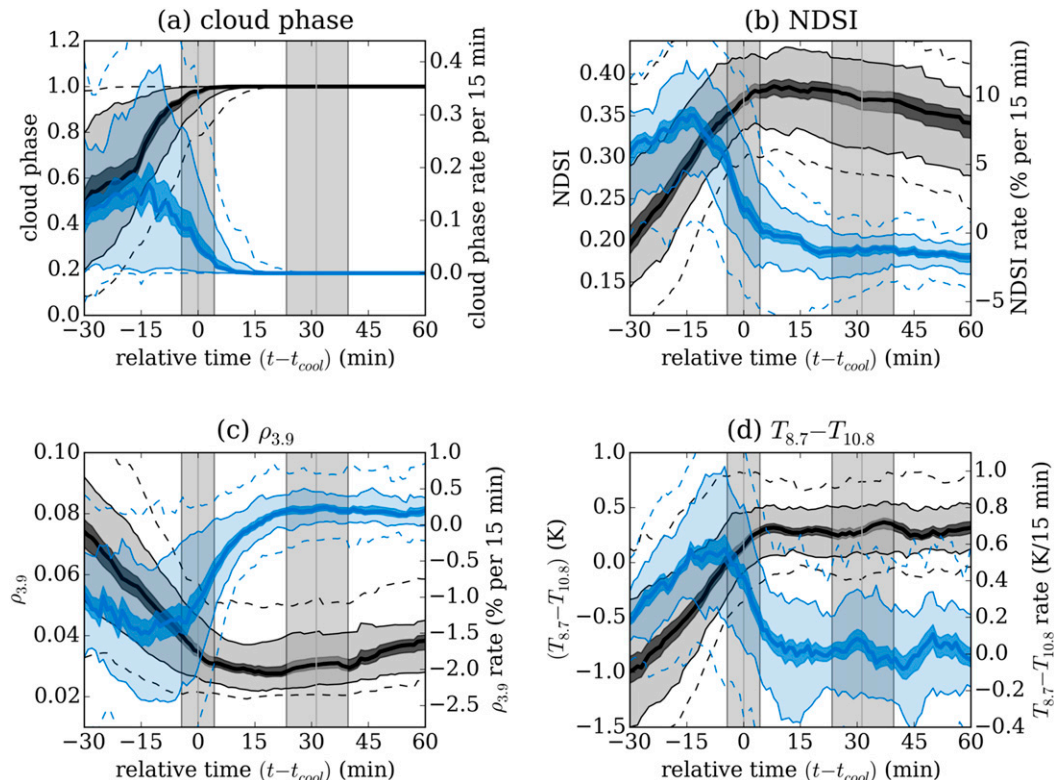


FIG. 4. As in Fig. 3, but for (a) cloud phase, (b) NDSI, (c)  $\rho_{3.9}$ , and (d)  $T_{8.7} - T_{10.8}$ . Cloud phase is retrieved by the cloud physical properties algorithm.

### b. Cloud-top microphysics and glaciation

In the following, we present an overview of the temporal evolution of several satellite-derived cloud-top products and radiance combinations that will be used to characterize the cloud-top microphysical state and the phase partitioning between liquid and frozen hydrometeors. A binary decision about the condensate phase is essentially inappropriate for the mixed-phase region of developing convective clouds, and cloud phase determination is highly uncertain. We therefore also consider radiance combinations that contain information about the phase partitioning within one pixel, which are approximately related to the ratio of total hydrometeor cross sections. The challenge, however, is that these kind of radiance combinations are also very sensitive to the size and habit of the considered hydrometeors (see, e.g., Baum et al. 2000). Furthermore, the depth of the considered cloud-top layer varies for different sensor wavelengths depending on the penetration depth of radiation (Platnick 2000).

Figure 4a shows the time series of cloud phase fraction, which is defined as the fraction of pixels classified as ice within the  $3 \times 3$  region around the satellite-based track. The average phase fraction starts around 0.5 at

$t_{\text{rel}} = -30$  min and increases up to 1 until  $t_{\text{rel}} = 0$ . Based on the classification of the CPP algorithm, cloud-tops of convectively growing clouds are fully glaciated at the time of maximum CTC. The temporal delay between CTC and glaciation indicates that release of latent heat of freezing prior to the time of maximum CTC is important to invigorate convective updrafts. This is in line with, for instance, Zipser (2003), who discussed the role of convective invigoration by freezing to balance entrainment in tropical convection, and also with Mecikalski et al. (2016), who investigated the relationship between convective updrafts and cloud-top glaciation with a similar combination of satellite observations, but with the very high temporal resolution of 1 min.

In addition, Fig. 4b gives the difference in solar reflectances  $\rho_{0.6}$  and  $\rho_{1.6}$  divided by their sum  $\rho_{0.6} + \rho_{1.6}$ . This quantity is often called normalized difference snow index (NDSI) and used to identify snow-covered land surfaces (Hall et al. 2002). It is, however, also a skillful quantity for the characterization of the cloud thermodynamical state. By construction, NDSI is less sensitive to optical thickness. The quantity increases for decreasing  $\rho_{1.6}$  and hence reflects the increase of ice fraction. The average NDSI curve strongly increases before maximum CTC and slightly decreases again



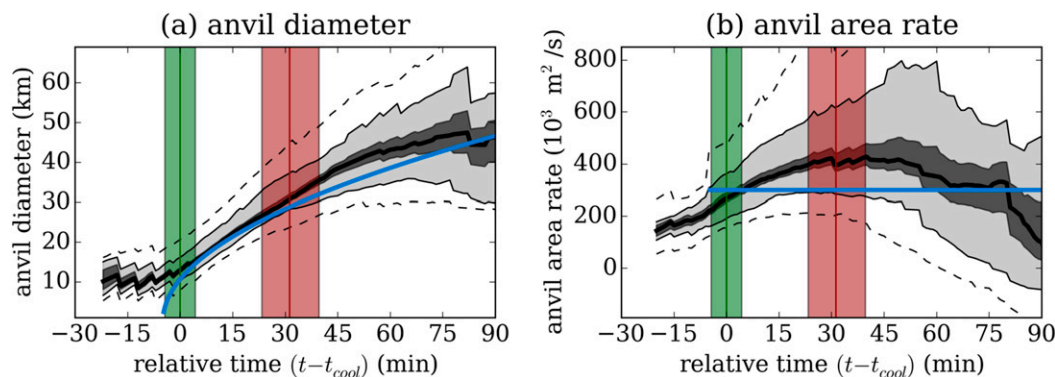


FIG. 5. As in Fig. 3, but for (a) anvil diameter and (b) anvil area rate. Time of maximum CTC and maturation time have been marked with green and red intervals, respectively. The anvil is defined as connected area with  $T_{10.8} < 240$  K. The light-blue curves show a simplified estimate of anvil changes in the case of the constant area rate of  $\alpha_0 = 300 \times 10^3 \text{ m}^2 \text{ s}^{-1}$ .

thereafter. The initial increase can be attributed to a change in phase partition and hence glaciation within the growing cloud. The later decrease in the considered quantity is likely attributable to a reduction of ice crystal size. Please note, however, that crystal habit can be quite variable in cirrus clouds and can depend on the strength of the anvil outflow [see, e.g., Wendisch et al. (2016) for a recent assessment]. In addition, Fig. 4c shows the evolution of  $\rho_{3.9}$ . The reflected solar radiance at  $3.9 \mu\text{m}$  drops down from 8% to around 3% as a result of increased absorption by ice. In the period thereafter,  $\rho_{3.9}$  starts to increase again because of decreasing particle sizes (Rosenfeld and Lensky 1998; Lindsey et al. 2006). Finally, Fig. 4d depicts an infrared measure of glaciation. The difference  $T_{8.7} - T_{10.8}$  is increasing from  $-1$  to  $0.3$  K during the initial updraft intensification period and remains approximately constant thereafter. The spread of  $T_{8.7} - T_{10.8}$  decreases significantly as a function of  $t_{\text{rel}}$ . Furthermore,  $T_{8.7} - T_{10.8}$  is less affected by ice-particle size for  $t_{\text{rel}} > 0$  possibly because of the balancing effects of particle size decrease and optical thickness increase.

The 5-min time trends of cloud phase fraction and the previously discussed radiance combination are also depicted in Fig. 4. The rates connected to solar reflectances (cloud phase rate in Fig. 4a, NDSI rate in Fig. 4b, and  $\rho_{3.9}$  rate in Fig. 4c) show a broad maximum centered around  $t_{\text{rel}} = -15$  min with a half-maximum width of around 30 min. This time rate signal is interpreted as a signature of glaciation rate. We infer that typical glaciation rates can be on the order of 20% per 15 min. In contrast, the  $T_{8.7} - T_{10.8}$  rates peak closer to the maximum CTC time at around  $t_{\text{rel}} = -5$  min and approach values around zero thereafter. Please note that the considered proxies for microphysical changes in the solar channels are much more certain in

the later mature phase than their infrared counterparts. This fact further supports the potential benefit of using solar information in convection nowcasting whenever possible.

### c. Anvil formation

Deep convective clouds develop cirrus anvils as a result of a converging vertical mass flux close to the tropopause, or equivalently another equilibrium level. By mass conservation, air has to diverge horizontally. The spreading anvil is easily detected in satellite observations and its expansion rate contains information about the strength of convective updrafts as well as compensating downdrafts within the cloud interior (see derivations in appendix B).

Figure 5 shows the properties of our case set related to anvil size and expansion. Figure 5a displays the median anvil diameter, which increases from around 10 km at time of maximum CTC up to 30 and 45 km at 30 and 60 min, respectively. The behavior of the anvil diameter before and in the vicinity of  $t_{\text{rel}} = 0$  is likely influenced by the complex cloud-top morphology of the still vertically growing convective cloud clusters. It was shown, for instance, by Adler and Fenn (1979a), that the vertical shift of sloped BT isolines leads to an apparent change in anvil size when a threshold-based anvil detection method is used. In Fig. 5b, the anvil area rates have a relatively small spread close to the time of maximum CTC. Initial values of  $250 \times 10^3 \text{ m}^2 \text{ s}^{-1}$  significantly increase within half an hour. The initial increase in area rate starts to stagnate at maturation time, and a broad maximum is reached between  $t_{\text{rel}} = 30$  and 50 min. After  $t_{\text{rel}} = 90$  min, anvil areas begin to shrink again. The typical relative increase in anvil area rate is a factor of 1.5, and more than 40% of the cases at least double their area rate within 60 min.



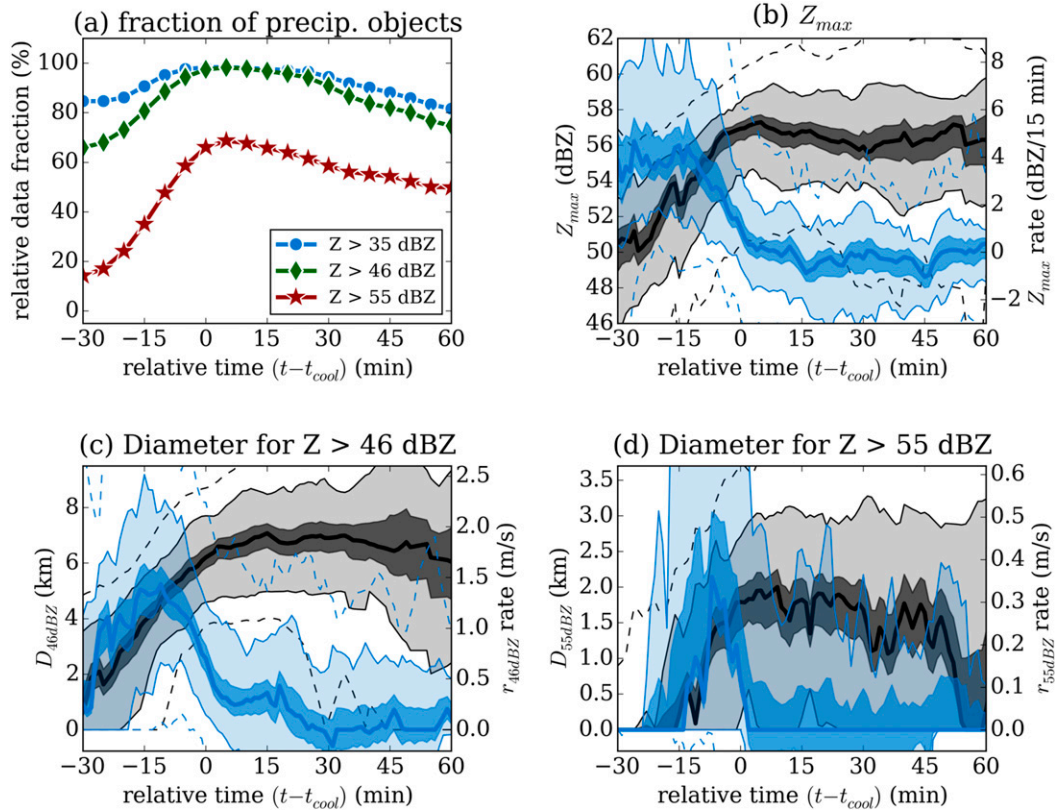


FIG. 6. As in Fig. 3, but for the characteristics of radar-derived precipitation objects. (a) The fraction of precipitation objects conditioned on different maximum  $Z$  intensities relative to the total number of tracks points with valid radar data. Further shown are (b) cell maximum radar reflectivity  $Z_{\max}$ , (c) equivalent cell diameters with  $Z > 46$  dBZ, and corresponding temporal rates. (d) Similar to (c), but for  $Z > 55$  dBZ.

We further provide estimates of median anvil behavior in case of a hypothetical, time-constant vertical mass flux in the different panels of Fig. 5. In a stationary setting, the anvil area  $A$  is supposed to increase linearly in time, that is,  $A \sim t_{\text{rel}} - t_0$ , where  $t_0$  is the time of zero anvil size (cf. appendix C). The anvil diameter and the anvil edge velocity thus scale like  $D \sim (t_{\text{rel}} - t_0)^{1/2}$  and  $u_r \sim (t_{\text{rel}} - t_0)^{-1/2}$ . By inspecting Fig. 5, we thus observe that the anvil properties significantly deviate from the curves expected for constant mass flux. Hence, the in-cloud mass flux is highly nonstationary and seems to increase by a factor of 1.5 on average within the 45-min period after the maximum of CTC.

#### d. Precipitation formation

The temporal evolution of radar-derived precipitation objects is analyzed here. First, the fraction of the precipitation cells relative to the number of cases with valid satellite and radar data is shown in Fig. 6a. Around 80% of the precipitation objects already exist at  $t_{\text{rel}} = -30$  min and thus have  $z$  values larger than 35 dBZ. In addition, around 65% (15%) of the cases

achieve reflectivities larger than 46 dBZ (55 dBZ) at  $t_{\text{rel}} = -30$  min. At the time of maximum CTC, two-thirds of the considered storm tracks show significant  $Z$  values above 55 dBZ. Hence, the probability is high that significant precipitation already exists at this stage of convective growth as characterized from the satellite perspective.

In addition, Fig. 6 presents the evolution of maximum precipitation cell reflectivity  $Z_{\max}$ , the equivalent object diameters  $D_{46\text{dBZ}}$  and  $D_{55\text{dBZ}}$ , and their time rates. The maximum  $Z$  values (Fig. 6b) reach 50 dBZ at  $t_{\text{rel}} = -30$  min and increase thereafter until the time of maximum CTC. The peak values reach on average 57 dBZ at  $t_{\text{rel}} = 5$  min, and slightly decrease afterward. The  $Z_{\max}$  rates (also in Fig. 6b) exhibit a broad maximum of around 4 dBZ per 15 min between 10 to 25 min before the maximum in CTC. After  $t_{\text{rel}} = 0$ , the  $Z_{\max}$  rates decrease significantly, and finally approach zero. The average diameter for cells with  $Z > 46$  dBZ is 2 km at  $t_{\text{rel}} = -30$  min and about 60% of the cases have cell diameters larger than 1 km at this early time instance. The 46-dBZ diameter steadily increases during the early

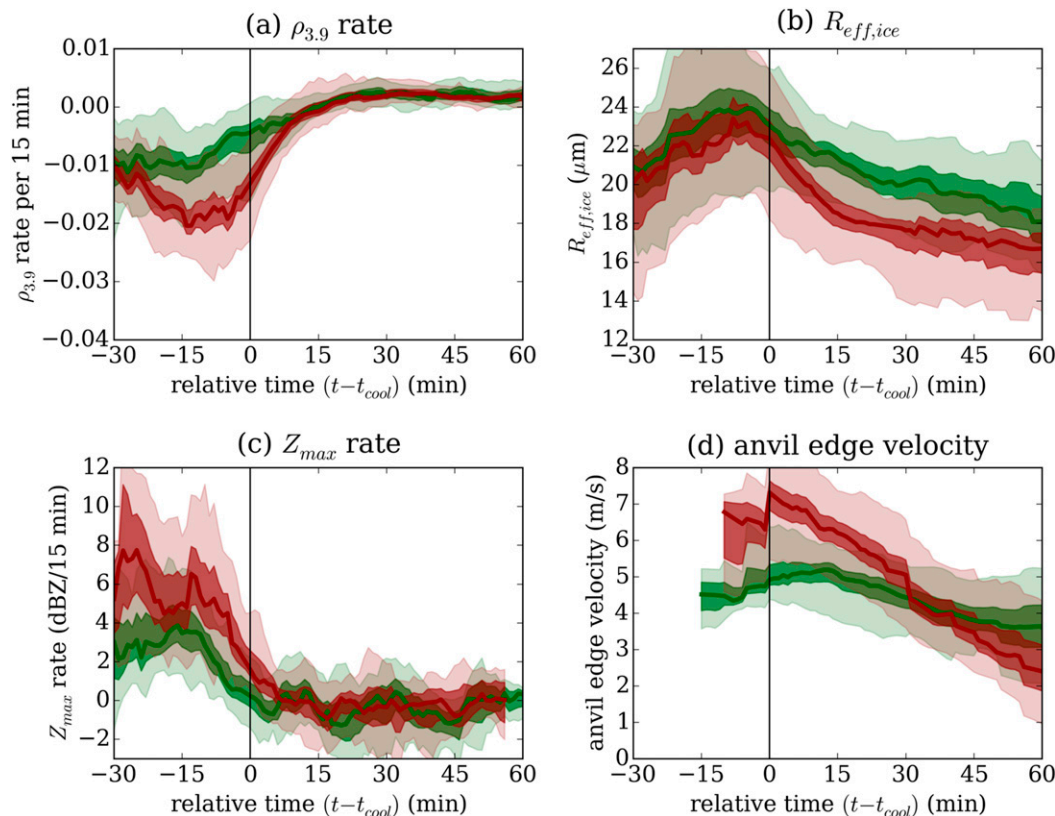


FIG. 7. Temporal evolution of (a)  $\rho_{3,9}$  rate, (b) effective radius of ice particles  $R_{\text{eff},\text{ice}}$ , (c)  $Z_{\text{max}}$  rate, and (d) anvil edge velocity for two different case subsets. The case-to-case median in maximum CTC rate is chosen to separate the weak-growth subset (green) from the strong-growth subset (red). The light and dark shaded intervals are similarly chosen as in Fig. 3.

updraft intensification phase, reaching around 6 km in size at the time of maximum CTC. Thereafter, the curve starts to stagnate, and shows increasing variability at later times. At  $t_{\text{rel}} = 0$ , close to 100% of the considered cases show precipitation with reflectivities of  $Z > 46$  dBZ. Figure 6d gives the equivalent diameter for  $Z > 55$  dBZ. Close to  $t_{\text{rel}} = -20$  min, the average 55-dBZ diameter starts to significantly deviate from zero. It also increases during the updraft intensification phase up to 2 km, and then starts to decrease again.

Furthermore, Figs. 6c and 6d show the time rate of the radii ( $r_{46\text{dBZ}}$  or  $r_{55\text{dBZ}}$ ) of the precipitation objects. This quantity would be equal to the cell edge velocity for circular objects but is still very useful to characterize the growth of realistic precipitation clusters with more complex shapes. The  $r_{46\text{dBZ}}$  rates have average values around  $0.5 \text{ m s}^{-1}$  at  $t_{\text{rel}} = -30$  min, and increase to a broad maximum centered around  $-15$  min, with peak values around  $1.5 \text{ m s}^{-1}$ . The following decrease in  $r_{46\text{dBZ}}$  rates already levels off within the satellite-determined growth phase. The  $r_{55\text{dBZ}}$  rates show a continued increase, starting around  $t_{\text{rel}} = -20$  min and reaching peak

values of  $0.5 \text{ m s}^{-1}$  close to the time of maximum CTC. We also see a sharp decrease in  $r_{55\text{dBZ}}$  rates thereafter, and no common trend for the case set during the continued growth period and after maturation time. The large variability in  $r_{55\text{dBZ}}$  rates shows that the satellite-based synchronization is unable to capture all relevant cloud-internal processes leading to heavy precipitation formation.

#### e. Weak versus strong growth

This subsection contrasts the temporal evolution of convective cloud and precipitation characteristics for two disjunct subsets of our set of storm cases corresponding to weak versus strong growth. The median of the maximum CTC rate with a value of 17 K per 15 min for all cases is chosen as discriminator to separate the subsets, with cases having a maximum CTC rate smaller than the median assigned to a “weak growth” subset, and a maximum CTC rate larger than the median to the “strong growth” subset. Figure 7a shows that the  $\rho_{3,9}$  rate as an indicator of the glaciation rate is significantly different in the two subsets. The strong-growth subset

shows a higher glaciation rate signature, which also peaks closer to the time of maximum CTC. The effective ice-particle radius  $R_{\text{eff,ice}}$  (in Fig. 7b) is not significantly different during the initial updraft intensification period for the two subsets. Radius  $R_{\text{eff,ice}}$  steadily increases during the first part of the growth phase and reaches a maximum at around  $t_{\text{rel}} = -5$  min and  $24 \mu\text{m}$ . The initial increase in  $R_{\text{eff,ice}}$  might be a signature of glaciation for which pixels containing liquid-water or mixed-phase clouds are already classified as ice phase. As liquid drops are less absorbing at  $1.6\text{-}\mu\text{m}$  wavelength than ice crystals of the same size, this results in a smaller apparent crystal size because of the lower absorption. As ice fraction increases, this effect becomes less important, and finally a maximum is reached. Thereafter,  $R_{\text{eff,ice}}$  decreases again and becomes  $2\text{--}3 \mu\text{m}$  smaller in the strong-growth subset. Rosenfeld et al. (2008b) discussed that small ice crystals in developing anvils indicate an increased probability of homogeneous freezing processes also as a result of smaller cloud-droplet residence times within strong updrafts (also see Lindsey et al. 2006). The rate of change of the maximum precipitation intensity (in Fig. 7c) is also much larger for the strong-growth subset, especially in the early growth phase, where up to twice as large  $Z_{\text{max}}$  rates can be found. However, the temporal change of precipitation exhibits a large uncertainty. Finally, Fig. 7d shows a measure for the anvil expansion. We have chosen the anvil edge velocity  $u_r$ , which characterizes the average apparent motion of the anvil edge in a storm-relative frame. In the beginning of the continued growth period,  $u_r$  is much larger for the strong-growth subset; for example, compare 7 with  $5 \text{ m s}^{-1}$  at  $t_{\text{rel}} = 5$  min. The anvil edge velocity decreases subsequently, with values eventually approaching around  $2.5 \text{ m s}^{-1}$  at  $t_{\text{rel}} = 60$  min for the strong-growth subset as compared with  $3.5 \text{ m s}^{-1}$  for the weak-growth subset.

#### f. Synthesis

Figure 8 presents a schematic view of the convective growth phase, combined with satellite-derived glaciation and growth rate as well as changes in precipitation intensity and core size. Two glaciation indicators, based on the CPP phase fraction rate and  $\rho_{3.9}$  rate, respectively, have significant values at  $-30$  min and reach their maximum between  $-15$  and  $-20$  min. The change in maximum precipitation intensity, shown by  $Z_{\text{max}}$  rates, mainly follows the change in satellite-derived glaciation indicators. At the maximum of the glaciation rates, heavy precipitation, shown by the  $r_{55\text{dBZ}}$  rate, has already set in. After a more or less steady increase, the  $r_{55\text{dBZ}}$  rate reaches its maximum around 5 min before the maximum in CTC. This highlights the implications

for nowcasting techniques using satellite information for CI detection. On the one hand, the sensitivity to cloud growth is much lower than to glaciation for obtaining meaningful lead times before the onset of precipitation. Going backward in time, cooling rates are a factor of 4 lower than their maximum values at  $t_{\text{rel}} = -30$  min. In contrast, glaciation rates are reduced only by a factor of around 1.5. On the other hand, glaciation rate estimates show a significantly larger along-track uncertainty than cloud-top cooling rates.

The average temporal evolution of convective growth, glaciation, and anvil properties reported so far is relatively robust and can also be reproduced when the time interval between the available satellite observations is increased from 5 to 15 min. Therefore, we have artificially decreased the temporal sampling frequency of the satellite-based properties to 15 min similar to the operational Meteosat prime service. Satellite-based time rates have been recalculated from 15-min differences, and synchronization of the storm tracks has been carried out based on the maximum CTC rates available at 15-min intervals. Thus, the alignment of along-track radar data is also affected, which has been kept at 5-min time resolution. With this setup, the temporal evolution of storm characteristics discussed previously was reproduced with similar behavior and magnitudes. As expected, a reduced accuracy and much higher uncertainty is found, however, which highlights the importance of a high temporal sampling frequency for nowcasting applications.

#### g. Cross correlations

Finally, we focus on the investigation of the interrelationships between different convective storm characteristics. For instance, the CTC rate and anvil edge velocity are expected to be linked by mass conservation. However, intrinsic differences between the initial motion of the cloud-top edge and the subsequent intensification of the cloud-internal mass flux might partly obscure any connection. Figure 9a displays the cross correlation between the maximum CTC rate derived at  $t_{\text{rel}} = 0$  and the anvil edge velocity  $u_r$  as function of relative time  $t_{\text{rel}}$ . For ease of visualization, we have converted the cooling rate into a vertical velocity estimate  $w_{\text{max}}$  using a constant lapse rate of  $7.6 \text{ K km}^{-1}$ , which is the average lapse computed in Senf et al. (2015). Please note that, because of sensor resolution limitations and our applied analysis strategy, the vertical velocities represent the ascent speed of convective cloud clusters averaged over a scale of  $10\text{--}15 \text{ km}$ , rather than the cloud-top motion of single convective towers. The observed correlation is positive and significant between  $t_{\text{rel}} = -5$  to  $30$  min. After around half an hour, information about the initial updraft speed is gone. A maximum correlation of around 0.55 indicates that

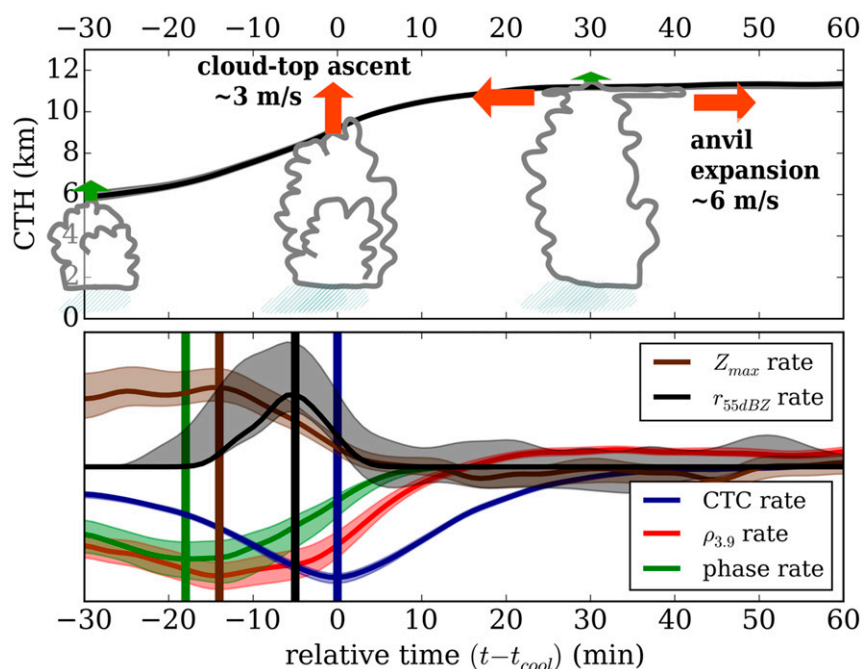


FIG. 8. (top) Schematic view on stages in the convective growth phase. Typical values of cloud-top ascent and anvil expansion velocities are indicated. (bottom) Combination of the case-to-case median of cloud phase rate (green) and  $\rho_{3.9}$  rate (red) as glaciation rate indicators, CTC rate (blue),  $Z_{max}$  rate (brown), and equivalent radar cell radius rate (black) as cloud growth and precipitation intensity change indicators, respectively. For ease of visualization, all satellite-based rates have been shown as negative values. An estimate of the confidence interval of the median calculated from the interquartile range divided by the square root of the number of the individually involved cases is shown by semitransparent shaded intervals. The time of the maximum/minimum is marked by a thick vertical line with the respective color.

approximately 305 of the variability in  $u_r$  can be explained with  $w_{max}$ . In addition, Fig. 9b shows the scatterplot of  $w_{max}$  versus  $u_r$  for  $t_{rel} = 8$  min, the moment when the smallest  $p$  value of the Spearman rank correlation coefficient is found [see, e.g., von Storch and Zwiers (2002) for definition]. The outward anvil motion is about twice as large as the vertical ascent speed measured with SEVIRI's sensor resolution. As both quantities can be derived only with significant uncertainties (see the error bars in Fig. 9b), we like to emphasize that a synergistic use of  $w_{max}$  together with  $u_r$  seems to be promising for now-casting applications.

The connection between cloud microphysical properties and growth characteristics is illustrated in Figs. 9c and 9d. The cross correlation between  $w_{max}$  and  $R_{eff,ice}$  decreases and attains significant values around  $-0.4$  between 10 and 40 min, which relates to an explained variance of only 16%. The smallest  $p$  value of the Spearman rank correlation is found at 23 min, for which a scatterplot is shown in Fig. 9d. There is significant spread between the variables, which can be partly explained by the intrinsic uncertainties in along-track

properties. However, for the strongest updrafts, ice particles at the cloud top are on average  $4 \mu\text{m}$  smaller than for the weakest updrafts. The weak anticorrelation between  $w_{max}$  and  $R_{eff,ice}$  is physically plausible and could result because ice particles may form later and have less time to grow in stronger updrafts. This is again in line with Rosenfeld et al. (2008b), who showed smaller ice crystals can serve as indicator for the severity of convective storms.

As a third cross-correlation example, Figs. 9e and 9f present the connection between satellite-based glaciation measures and the subsequent precipitation intensity. As a glaciation indicator, the  $\rho_{3.9}$  rate at  $t_{rel} = -10$  min was selected, which is the time when the stronger-growing storms show a maximum in the  $\rho_{3.9}$  rate (see Fig. 7a). Reflectivity  $Z_{max}$  has been evaluated for different relative times  $t_{rel} > -10$  min. The cross correlation decreases throughout the growth phase and becomes significant around the time of maturation. Hence, storms that possess larger glaciation rates also produce higher peak precipitation intensities at the beginning of the mature phase. Please note that the discussed relationship



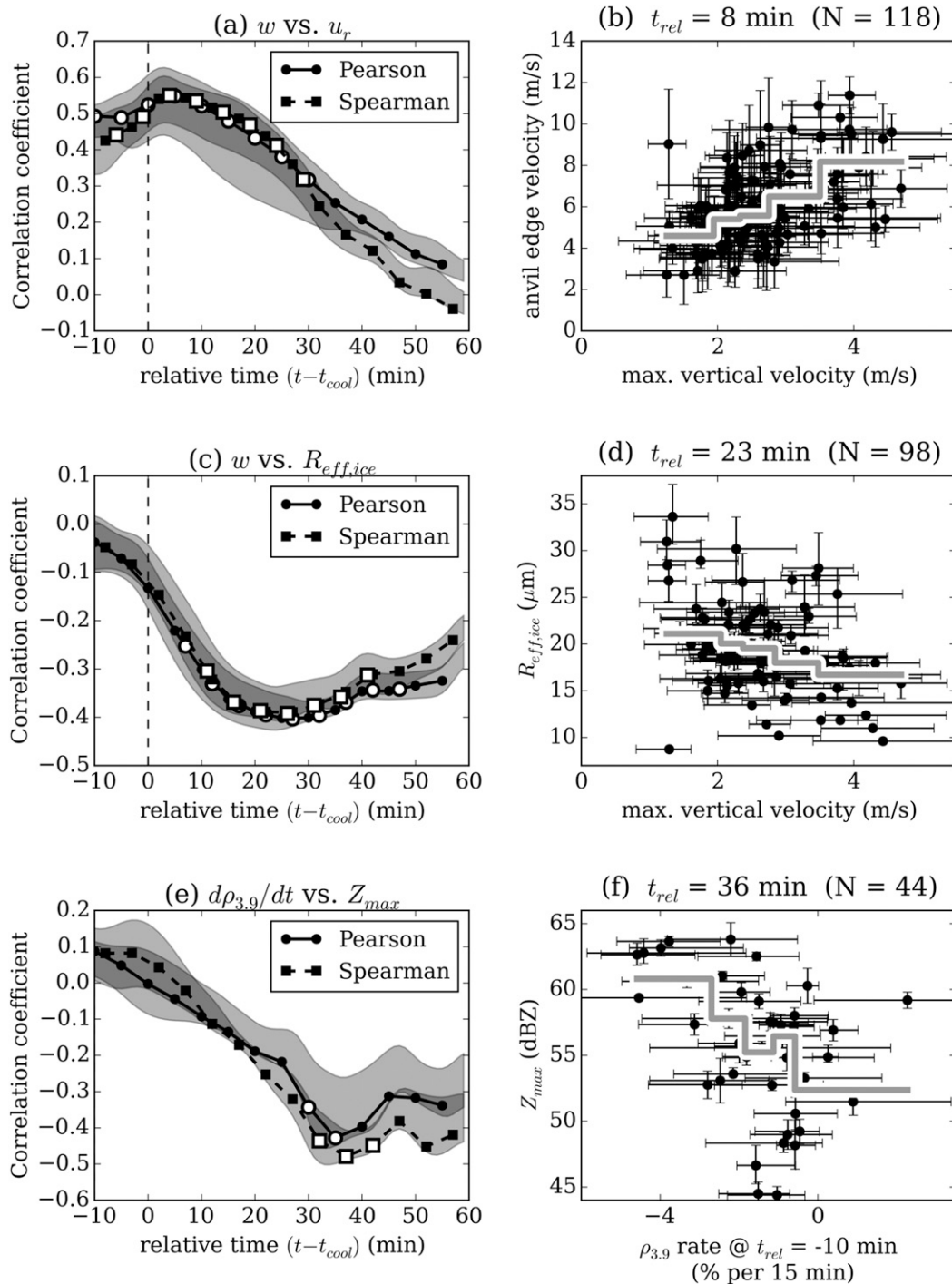


FIG. 9. (left) Cross correlation between two variables: the first one selected at fixed relative time and the second one sequentially evaluated at different times  $t_{rel}$ . CTC rate at  $t_{rel} = 0$  combined with (a) anvil edge velocity  $u_r$  and (c)  $R_{eff,ice}$ ; (e) the  $\rho_{3,9}$  rate selected at  $t_{rel} = -10$  min together with  $Z_{max}$  as function of time. Two measures of linear correlation (Pearson correlation coefficient with circles and solid line, and Spearman rank correlation coefficient with squares and dashed line) are plotted. The semitransparent gray-shaded intervals give the minimum-maximum range in correlation coefficient obtained by successive permutation of the 25th, 50th, and 75th percentiles of each variable. Open symbols are plotted for correlations with maximum  $p$  values less than 0.01 indicating 1% significance. (right) Scatterplot of (b) maximum CTC rate vs  $u_r$  at  $t_{rel} = 8$  min, (d) maximum CTC rate vs  $R_{eff,ice}$  at  $t_{rel} = 23$  min, and (f)  $\rho_{3,9}$  rate at  $t_{rel} = -10$  min vs  $Z_{max}$  at  $t_{rel} = 36$  min. CTC rates are converted to velocity units (as  $w$ ) using a constant temperature lapse rate of  $7.6 \text{ K km}^{-1}$ . Error bars indicate variable interquartile range. Thick gray lines indicate the sequential median of data pair in 20th percentile intervals of the abscissa variable.

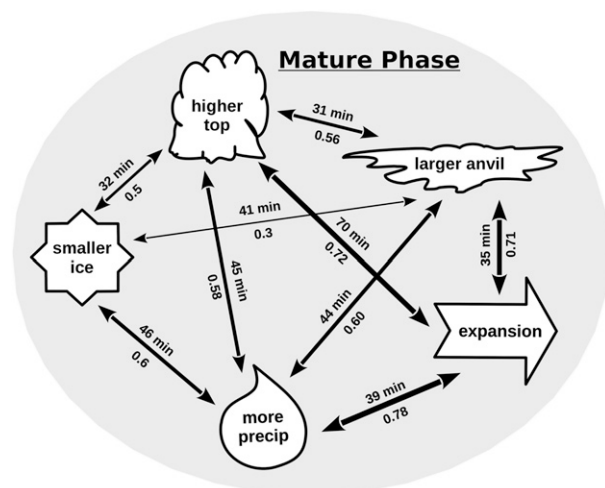


FIG. 10. Sketch of connections between convective cloud and precipitation characteristics within the mature phase. Solid lines mark simultaneous cross correlations between storm properties at fixed relative times, which are indicated above the lines. The linear correlation value is given below the connection lines. Similar to Fig. 9, only the time and the corresponding correlation at minimum  $p$  value is indicated. Note however, that the cross-correlation values can have a broad time range in which significant values are obtained.

involves a lead time of 46 min. However, further research is needed to fully evaluate the skill of the  $\rho_{3,9}$  rate for nowcasting of precipitation intensity.

We conclude the section with a discussion of interrelationships between storm properties at the beginning of the mature phase. A sketch is shown in Fig. 10, where we have analyzed the instantaneous cross correlations between combinations of satellite-based and radar-derived storm characteristics. Each arrow in Fig. 10 represents a scatterplot evaluated at a certain time, which is indicated above the arrow. At this time, the highest statistical significance is found for the observed cross correlation between two connected variables. The thickness of the arrow and the number below the arrow indicate the magnitude of this cross correlation. Either  $D_{55\text{dBZ}}$  or  $Z_{\text{max}}$  is chosen as the measure of precipitation intensity. These two radar-derived variables are closely connected and attain cross-correlation values typically greater than 0.9 throughout the beginning mature phase (not shown). For higher precipitation intensities, we find on average smaller ice crystals and colder convective core temperatures at the cloud top. Furthermore, anvil shields become larger and show higher expansion rates for storms with heavier precipitation.

## 5. Conclusions

We have investigated the growth phase of developing convective storms and their transition to maturity. The

study is based on a synergistic combination of cloud-top signatures from geostationary satellite and precipitation intensity estimates from a ground-based radar network. The major goals of the study are 1) to show the satellite-derived characteristics of growing cloud tops and illuminate interrelationships between cloud depth, growth, and glaciation properties depending on the stage within the growth phase, 2) to investigate the timing of the onset and subsequent change to moderate and heavy intensity of the radar-derived precipitation with respect to satellite-based growth and glaciation processes, and 3) to show and discuss implications for satellite-based nowcasting of convective initiation (CI), when a generalization seems to be reasonable.

For the characterization of convective development from satellite, we have used solar reflectances, infrared BTs, and cloud products from the SEVIRI instrument on board the geostationary Meteosat satellites. Dynamical growth properties have been studied based on cloud-top cooling (CTC) rates and anvil expansion speeds. Cloud-top glaciation has been estimated based on several multispectral measures: cloud phase fraction, solar reflectances at 1.6 and  $3.9\mu\text{m}$ , and a combination of brightness temperatures at 8.7, 10.8, and  $12\mu\text{m}$ . A gridded composite of radar reflectivities has been obtained from surface precipitation scans of the German radar network.

One major advantage of the two observational systems for the characterization of convective growth is their high scan frequency of 5 min, which allows us to calculate Lagrangian changes of cloud and precipitation properties at high temporal resolution. More than 100 satellite-based convective storm tracks have been determined and analyzed for the years 2012–14 and the region of central Europe. For most of the investigated cases, we find that the CTC rate shows a pronounced maximum during the growth phase. The time of the maximum CTC has been utilized to synchronize the satellite-derived and radar-based storm properties. The main findings of the analysis of these properties are summarized as follows:

- (i) The satellite-derived growth duration, determined by the half-maximum width of the CTC rate, lasts around half an hour, at least for the spatial resolution of Meteosat SEVIRI. A good correlation between CTC and anvil edge velocity exists, suggesting that a synergistic use of the satellite-based growth properties might be beneficial for nowcasting applications.
- (ii) Anvil properties, computed from connected areas of  $10.8\text{-}\mu\text{m}$  brightness temperatures less than 240 K, deviate significantly from properties expected for constant vertical mass flux. Ignoring

anvil thinning by particle sublimation, we infer that the in-cloud mass flux is highly nonstationary and seems to increase by a factor of 1.5 on average within 45 min after the maximum in CTC, which is likely caused by an increase of the updraft core size.

- (iii) Satellite-based glaciation rate estimates reach a maximum 15 min prior to the maximum in CTC, indicating that release of latent heat of freezing prior to the maximum is important to invigorate convective updrafts.
- (iv) We find a weak connection between maximum CTC magnitude during the growth phase and ice-particle size in the mature phase. Slightly smaller particles are retrieved for larger cloud-top ascent velocities. We interpret this as an observable indication that ice particles may form later and may have less time to grow in stronger convective updrafts.
- (v) Furthermore, higher maximum precipitation intensities and larger precipitation cores are found for mature convective clouds with higher cloud tops, larger anvil sizes and expansion rates, and smaller ice crystals in the cloud-top region.
- (vi) By investigating the onset of precipitation in relation to CTC signatures, we find that the probability is large that significant precipitation already exists at an early stage of satellite-derived convective growth. Satellite-based techniques for early CI detection therefore have to target the early updraft intensification period 30 min prior to the maximum in CTC. Moreover, information from solar channels should be used whenever possible to obtain an increased accuracy for inferring cloud-top glaciation from satellite observations.

Our study has aimed at identifying common features in the convective growth, without taking into account the impact of the environment on convective strength and organization. We expect, however, that some part of the uncertainty in our inferred relationships can be reduced by meaningful inclusion of environmental properties like convective instability, moisture supply, and flow characteristics, which is planned for future analyses. Moreover, we hope to attribute modifications of convective growth and glaciation processes to changes in aerosol load, a challenge to clarify a potentially important anthropogenic influence on convection and climate (Rosenfeld et al. 2008a). We further aim to incorporate observations from lightning networks in future research to increase our understanding of the relationships between multispectral cloud-top signatures from satellite and the accompanying hazards of thunderstorms.

We also like to stress that a further quantification and validation of Meteosat-based CI capabilities for the

central European domain is needed. Concerning operational nowcasting in general, we see our study as a guide on which future conceptual models of the life cycle of convection can be built that combine temporal changes in satellite- and radar-based proxies of convective activity. Challenges for the application in operational environments are related to the quality of the automated detection of convective clouds, the tracking methods, and the discrimination of strong convective growth and other measures of storm severity from signatures that might arise from algorithm artifacts. However, not all these important issues have been treated in our current study and are left for future efforts.

*Acknowledgments.* The work has been partially conducted within the OASE project of the Hans Ertel Center for Weather Research, coordinated by the German Weather Service and funded under Grant T1-A9-EZ-2011b, as well as within the HD(CP)<sup>2</sup> project funded by the BMBF under Grant 01LK1507C. We thank three anonymous reviewers, whose comments helped to improve the manuscript. We acknowledge EUMETSAT for providing SEVIRI data and DWD for providing the Radolan RX composites. Special thanks are given also to the members of the EUMETSAT convection working group for stimulating discussions.

## APPENDIX A

### Details on Tracking Methodology

#### *a. Construction of satellite-based tracks and along-track properties*

The satellite-based tracks are constructed in two steps. In the first step, automatic detection and tracking of convective anvils is performed. For detection, the observed  $T_{10.8}$  field has been masked with a threshold value of 230 K for each satellite image during the summer half-years of 2012–14. The resulting two-dimensional binary masks are segmented into cell objects using a 4-connectivity clustering algorithm. For each cell object, the cell area and the equivalent diameter is calculated, the latter representing the diameter of a hypothetical equal-area circle. Cells with an equivalent diameter between 20 and 30 km are selected for anvil tracking. Following Senf et al. (2015), this size range corresponds to growing convective cells in the continued growth period after the time of maximum CTC and before the time of maturation. Thereafter, the masking and segmentation of the  $T_{10.8}$  field is repeated with a threshold value of 240 K, which corresponds to the value taken for the manual determination of anvil characteristics in

Senf et al. (2015). Tracking based on cell overlap is performed using the connectivity of two consecutive binary masks along the temporal dimension in forward and backward directions. Because of the high temporal resolution of 5 min, no nowcasting step is needed to improve the overlap of considered cells.

In a second step, the automatically obtained tracks have been randomly shuffled. Thereafter, we started to sequentially extend the tracks manually into the early stages of the convective growth phase, with emphasis on spatial coherence in the  $T_{10.8}$  and—if available—also in the HRV fields. Extrapolation of the tracks backward into the very early stage of cumulus development is very challenging for an automated algorithm, which is the reason why we chose the same manual strategy for backward tracking as in our earlier study (Senf et al. 2015). After the number of tracks reached around 150, we stopped this time-consuming manual work as the number of cases was determined to be sufficient to obtain robust results. Please note that complicated splits or merges of convective cells were avoided in the manual analysis.

For calculation of along-track properties and rates, small cutouts (typically  $51 \times 51$  pixels) of satellite data and products are first obtained centered on the track positions and stacked in time. Second, masking of the 3D data cube with the cloud mask and type conditions as described in section 2, as well as solar illumination conditions for solar channels and cloud microphysical and optical properties, is applied. All the following analysis steps exclude invalid pixels from the calculations. In a third step, the masked data are smoothed with a Gaussian kernel of two pixels, one pixel, and 5-min width in the respective space and time dimensions. The filtering was chosen to enhance our ability to extract convective growth properties on temporal scales of 10 min or larger. We are aware that current studies show the improved capabilities of so-called superrapid scans with update cycles between 1 and 2.5 min to characterize the rapid parts of cumulus development (Mecikalski et al. 2016).

For derivation of along-track properties and to obtain quantitative estimates of uncertainty, we apply the method developed in Senf et al. (2015). We assume that the actual cell track can be misplaced by one pixel because of ambiguities in subsequent images and subpixel shifts. A  $3 \times 3$  core region centered around the track location is selected from the masked and filtered satellite data stack. Thereafter, a random-track set is generated by randomly choosing new track positions out of the respective  $3 \times 3$  region. The bootstrapping procedure is repeated 100 times. The median and interquartile range is calculated from the random-track set of each time step. In addition, we derive temporal rates from the random-track set using 5-min centered

differences. Please note that the calculated time rates have been rescaled by a factor of 3 to allow for easy comparison with existing literature, which usually presents rates in units per 15 min.

For the object-based anvil properties, smoothing of the time series with a Gaussian kernel of width 15 min is applied. This is especially important to reduce noise in the outward-pointing anvil edge velocity. For an uncertainty estimate, a running average is applied to the time series, and a running standard deviation with the same kernel width is computed.

### *b. Derivation of radar-based objects*

First, the tracks have been parallax corrected using the NWCSAF cloud-top-height product and standard routines. Next, along-track  $Z$  cutouts centered around the parallax-corrected track ( $121 \times 121$  grid boxes) are gathered and stacked in time and eventually masked with a threshold of 35 dBZ. Because of different spatial resolutions of satellite and radar data, as well as increasing apparent shifts due to cloud growth effects, it was found necessary to realign the radar data. We therefore successively performed image registration techniques that use maximum correlation to correct for apparent spatial shifts in the masked radar data. The realigned and masked radar data are smoothed in time, and precipitation clusters are determined by a combination of automatic clustering and manual selection described in the following.

In a first step, a 3D connectivity cluster algorithm was applied to the smoothed and realigned radar data. The cluster algorithm is built on a binary mask using a threshold of 35 dBZ. The cluster center position that was closest to the parallax-corrected satellite-based track and with meaningful temporal length was chosen as first guess of the 3D radar-based precipitation cluster. In a second step, a manual correction was performed to ensure a high quality of the precipitation cell dataset. We developed an interactive application in which radar fields and marked cell objects are visualized and highlighted simultaneously at different time instances. By hand, a human expert added missing or removed wrongly assigned parts of the radar fields.

## APPENDIX B

### **Relationship between Updraft Strength and Anvil Expansion**

A large body of literature exists showing the utility of the normalized anvil expansion rate  $A^{-1}D_t A$  for nowcasting severe storms, where  $A$  denotes the anvil area



and  $D_t$  denotes the Lagrangian time change. To name a few studies, [Adler and Fenn \(1979a\)](#) found in an early study that high normalized anvil expansion rates together with very cold minimum BTs are indicative of the severity of convective storms. [Machado et al. \(1998\)](#) and [Machado and Laurent \(2004\)](#) investigated the relationship between the initial normalized areal time rate of expansion and the total lifetimes of tropical convective systems. The authors showed that the area expansion is also a good indicator of convective activity, and that its initial value serves as a good predictor of the life time of convective systems. It has been further discussed that  $A^{-1}D_t A$  is closely related to the local divergence of horizontal flow  $\nabla_h \cdot \mathbf{u}$ , if changes in the anvil microphysical and hence radiative properties are negligible. It should be noted, however, that if  $A$  is not a small but rather a large area, the normalized expansion rates  $A^{-1}D_t A$  give instead the area-average horizontal divergence, that is,  $\langle \nabla_h \cdot \mathbf{u} \rangle_A$ . This property, however, shows an intrinsic decrease proportional to  $A^{-1}$  for situations with constant mass flux as a response as will be shown in the following.

To recapitulate the essential connection between updraft strength and anvil speed, we consider the mass conservation in anelastic approximation ([Vallis 2006](#))

$$r^{-1} \partial_r (r \bar{\rho} u_r) + \partial_z (\bar{\rho} w) = 0, \quad (\text{B1})$$

where we selected cylindrical coordinates. Moreover, we applied radial averaging to the velocities, which does not constrain the considerations to purely cylindrical clouds but still requires that the term “outward” is meaningfully defined with respect to the considered cloud frame. The terms  $r$  and  $z$  denote the radial and vertical coordinates, and  $\partial_r$  and  $\partial_z$  are the corresponding partial derivatives;  $\bar{\rho}$  is a typical reference or environmental air density,  $u_r$  is the average outward-pointing radial velocity, and  $w$  is the average vertical velocity. We now consider a hypothetical cylinder that is centered on the updraft maximum at  $r = 0$  and with mass flux  $\bar{\rho} w$ . We assume a cylinder of width  $r_c$  with its bottom level  $z_b$  at the height of maximum updraft and its top level  $z_t$  at zero vertical velocity. Then integration over the volume of the cylinder gives

$$r_c \int_{z_b}^{z_t} dz \bar{\rho} u_c = \int_0^{r_c} dr r \bar{\rho} w_b, \quad (\text{B2})$$

where  $u_c = u_c(t, z)$  is the outward-pointing velocity evaluated at cylinder edge  $r_c$ , and  $w_b = w_b(t, r)$  is the vertical velocity at the cylinder bottom level. Entrainment of environmental air is an important limiting factor for convective growth (see, e.g., [Houze 2014](#)). However,

if we ignore inward transport of environmental air for simplicity, the last equation just states that the area-averaged in-cloud mass flux must be compensated by an outward anvil expansion. We further assume that the updraft area  $A_w$  is comparably small to the cylinder-top area  $A_c$ . As a result, the layer-averaged outward-directed horizontal mass flux obeys

$$\langle \bar{\rho} u_c \rangle_h = \frac{A_w}{2\pi r_c h} \langle \bar{\rho} w_b \rangle_{A_w}. \quad (\text{B3})$$

In the last expression, the vertical depth of the anvil  $h$  is introduced, which might be significantly smaller than the cylinder height  $z_t - z_b$ . Additionally, horizontal averaging over the area  $A_w$  at  $z_b$  as well as vertical averaging over depth  $h$  at  $r_c$  is denoted by brackets with corresponding subscripts. Thus, the conversion factor between horizontal and vertical mass flux is given by the ratio of the updraft area  $A_w$  to the part of the cylinder area  $2\pi r_c h$  through which the anvil flows.

If we finally allow the hypothetical cylinder to change in time and attach it to the outward-directed flow, that is, assuming  $D_t r_c = u_c$ , where  $D_t$  gives the Lagrangian time change following the air trajectory, we obtain

$$\frac{2\pi r_c}{A_w} \langle \bar{\rho} D_t r_c \rangle_h = \frac{1}{A_w} \langle \bar{\rho} D_t A_c \rangle_h = \frac{1}{h} \langle \bar{\rho} w_b \rangle_{A_w}. \quad (\text{B4})$$

Equation (B4) is quite general and also holds for non-stationary condition with average mass flux  $\langle \bar{\rho} w_b \rangle_{A_w}$  changing in time. It could be even further generalized to capture multiple updraft cores and downdraft areas by translating  $A_w \langle \bar{\rho} w_b \rangle_{A_w}$  to  $A_{w,i} \langle \bar{\rho} w_b \rangle_{A_{w,i}}$  and applying summation over all different and disjoint areas  $A_{w,i}$ . We like to emphasize that the major limitation of Eq. (B4) is the neglect of lateral entrainment. Equation (B4) rather involves the ratio  $D_t A_c / A_w$  and not  $D_t A_c / A_c$  with the consequence of two interesting limits: The temporal change of the material area  $A_c$  is constant if, first, the average upward-directed mass flux is constant and, second, the area  $A_w$  occupied by the updraft remains constant. The satellite-derived anvil area  $A$  might be related to the material area  $A_c$  if sublimation of ice and also other processes that lead to changes in the anvil radiative properties can be neglected, which can be a severe simplification of real anvil behavior.

## APPENDIX C

### Anvil Expansion for Constant Vertical Mass Flux

For the reader's convenience, we give analytic solutions of the mass conservation Eq. (B4) in the case of a

temporally constant vertical mass flux. If we assume that the outflow air density is approximated by  $\rho_h$  and that the anvil area is attached to the flow, that is,  $\langle \bar{\rho} A_c \rangle_h = \bar{\rho}_h A$ , then Eq. (B4) is rearranged to

$$D_t A = \frac{A_w}{h} \frac{\bar{\rho}_b}{\bar{\rho}_h} \langle w_b \rangle_{A_w} \equiv \alpha_0, \quad (\text{C1})$$

where  $\bar{\rho}_b$  and  $w_b$  are evaluated at level  $z_b$ . If now the term on the right-hand side is constant, the anvil area obeys

$$A = \alpha_0 (t_{\text{rel}} - t_0), \quad (\text{C2})$$

where  $t_0$  marks the relative time when the anvil area vanishes. The anvil diameter

$$D = \sqrt{\frac{4}{\pi} \alpha_0 (t_{\text{rel}} - t_0)} \quad (\text{C3})$$

increases by the square root of relative time, whereas the anvil edge velocity is supposed to decrease with the inverse square root of time, that is,

$$u_r = \sqrt{\frac{1}{4\pi} \frac{\alpha_0}{t_{\text{rel}} - t_0}}. \quad (\text{C4})$$

Now, choosing the values that attach the theoretical curve to the median observation of Fig. 5a at  $t_{\text{rel}} = 5$  min, we obtain  $\alpha_0 = 300 \times 10^3 \text{ m}^2 \text{ s}^{-1}$  and  $t_0 = -5$  min. Assuming that the density in the vertical flow maximum  $\bar{\rho}_b$  is twice as large as the air density at anvil altitudes  $\bar{\rho}_h$ , and setting the ratio between updraft area  $A_w$  and anvil outflow thickness  $h$  to 5 km, the average updraft speed is  $\langle w_b \rangle_{A_w} = 25 \text{ m s}^{-1}$ , which is a plausible value (Lang and Rutledge 2002). This taken  $A_w/h$  ratio would, for instance, correspond to an anvil outflow thickness of 1 km and a core updraft radius of 700 m. This also makes clear that a temporal change in the anvil area rate by a factor of 2 or 3 is more likely caused by an increase of the updraft core size than an increase in vertical flow speed, which approaches certain limits governed by convectively available energy, entrainment, and mixing processes (Houze 2014).

## REFERENCES

- Adler, R. F., and D. D. Fenn, 1979a: Thunderstorm intensity as determined from satellite data. *J. Appl. Meteor.*, **18**, 502–517, doi:10.1175/1520-0450(1979)018<0502:TIADFS>2.0.CO;2.
- , and —, 1979b: Thunderstorm vertical velocities estimated from satellite data. *J. Atmos. Sci.*, **36**, 1747–1754, doi:10.1175/1520-0469(1979)036<1747:TVVEFS>2.0.CO;2.
- Baum, B. A., P. F. Soulen, K. I. Strabala, M. D. King, S. A. Ackerman, W. P. Menzel, and P. Yang, 2000: Remote sensing of cloud properties using MODIS airborne simulator imagery during SUCCESS: 2. Cloud thermodynamic phase. *J. Geophys. Res.*, **105**, 11 781–11 792, doi:10.1029/1999JD901090.
- Bley, S., and H. Deneke, 2013: A threshold-based cloud mask for the high-resolution visible channel of Meteosat second generation SEVIRI. *Atmos. Meas. Tech.*, **6**, 2713–2723, doi:10.5194/amt-6-2713-2013.
- Deneke, H. M., and R. A. Roebeling, 2010: Downscaling of METEOSAT SEVIRI 0.6 and 0.8  $\mu\text{m}$  channel radiances utilizing the high-resolution visible channel. *Atmos. Chem. Phys.*, **10**, 9761–9772, doi:10.5194/acp-10-9761-2010.
- Derrien, M., and H. Le Gléau, 2005: MSG/SEVIRI cloud mask and type from SAFNWC. *Int. J. Remote Sens.*, **26**, 4707–4732, doi:10.1080/01431160500166128.
- Hall, D. K., G. A. Riggs, V. V. Salomonson, N. E. DiGirolamo, and K. J. Bayr, 2002: MODIS snow-cover products. *Remote Sens. Environ.*, **83**, 181–194, doi:10.1016/S0034-4257(02)00095-0.
- Heymsfield, G. M., R. H. Blackmer Jr., and S. Schotz, 1983: Upper-level structure of Oklahoma tornadic storms on 2 May 1979. I: Radar and satellite observations. *J. Atmos. Sci.*, **40**, 1740–1755, doi:10.1175/1520-0469(1983)040<1740:ULSOOT>2.0.CO;2.
- Houze, R. A., 2014: *Cloud Dynamics*. International Geophysics Series, Vol. 104, Academic Press, 496 pp.
- Lang, T. J., and S. A. Rutledge, 2002: Relationships between convective storm kinematics, precipitation, and lightning. *Mon. Wea. Rev.*, **130**, 2492–2506, doi:10.1175/1520-0493(2002)130<2492:RBCSKP>2.0.CO;2.
- Lindsey, D. T., D. W. Hillger, L. Grasso, J. A. Knaff, and J. F. Dostalek, 2006: GOES climatology and analysis of thunderstorms with enhanced 3.9- $\mu\text{m}$  reflectivity. *Mon. Wea. Rev.*, **134**, 2342–2353, doi:10.1175/MWR3211.1.
- Machado, L. A. T., and H. Laurent, 2004: The convective system area expansion over Amazonia and its relationships with convective system life duration and high-level wind divergence. *Mon. Wea. Rev.*, **132**, 714–725, doi:10.1175/1520-0493(2004)132<0714:TCSAEO>2.0.CO;2.
- , W. Rossow, R. Guedes, and A. Walker, 1998: Life cycle variations of mesoscale convective systems over the Americas. *Mon. Wea. Rev.*, **126**, 1630–1654, doi:10.1175/1520-0493(1998)126<1630:LCVOMC>2.0.CO;2.
- Marshak, A., S. Platnick, T. Varnai, G. Wen, and R. F. Cahalan, 2006: Impact of three-dimensional radiative effects on satellite retrievals of cloud droplet sizes. *J. Geophys. Res.*, **111**, D09207, doi:10.1029/2005JD006686.
- Matthee, R., and J. R. Mecikalski, 2013: Geostationary infrared methods for detecting lightning-producing cumulonimbus clouds. *J. Geophys. Res. Atmos.*, **118**, 6580–6592, doi:10.1002/jgrd.50485.
- Mecikalski, J. R., and K. M. Bedka, 2006: Forecasting convective initiation by monitoring the evolution of moving cumulus in daytime GOES imagery. *Mon. Wea. Rev.*, **134**, 49–77, doi:10.1175/MWR3062.1.
- , —, S. J. Paech, and L. A. Litten, 2008: A statistical evaluation of GOES cloud-top properties for nowcasting convective initiation. *Mon. Wea. Rev.*, **136**, 4899–4914, doi:10.1175/2008MWR2352.1.
- , W. M. MacKenzie Jr., M. Koenig, and S. Muller, 2010a: Cloud-top properties of growing cumulus prior to convective initiation as measured by Meteosat Second Generation. Part I: Infrared fields. *J. Appl. Meteor. Climatol.*, **49**, 521–534, doi:10.1175/2009JAMC2344.1.
- , —, —, and —, 2010b: Cloud-top properties of growing cumulus prior to convective initiation as measured by

- Meteosat Second Generation. Part II: Use of visible reflectance. *J. Appl. Meteor. Climatol.*, **49**, 2544–2558, doi:[10.1175/2010JAMC2480.1](https://doi.org/10.1175/2010JAMC2480.1).
- , M. König, and C. P. Jewett, 2013a: Application of high-resolution visible sharpening of partly cloudy pixels in Meteosat Second Generation infrared imagery. *Atmos. Res.*, **134**, 1–11, doi:[10.1016/j.atmosres.2013.07.014](https://doi.org/10.1016/j.atmosres.2013.07.014).
- , P. Minnis, and R. Palikonda, 2013b: Use of satellite derived cloud properties to quantify growing cumulus beneath cirrus clouds. *Atmos. Res.*, **120**, 192–201, doi:[10.1016/j.atmosres.2012.08.017](https://doi.org/10.1016/j.atmosres.2012.08.017).
- , C. P. Jewett, J. M. Apke, and L. D. Carey, 2016: Analysis of cumulus cloud updrafts as observed with 1-minute resolution super rapid scan goes imagery. *Mon. Wea. Rev.*, **144**, 811–830, doi:[10.1175/MWR-D-14-00399.1](https://doi.org/10.1175/MWR-D-14-00399.1).
- Meirink, J. F., R. Roebeling, E. Wolters, and H. Deneke, 2010: Cloud physical properties: SEVIRI/AVHRR. Algorithm Theoretical Basis Doc. SAF/CM/KNMI/ATBD/CPP, 23 pp.
- Merk, D., and T. Zinner, 2013: Detection of convective initiation using Meteosat SEVIRI: Implementation in and verification with the tracking and nowcasting algorithm Cb-TRAM. *Atmos. Meas. Tech.*, **6**, 1903–1918, doi:[10.5194/amt-6-1903-2013](https://doi.org/10.5194/amt-6-1903-2013).
- Nakajima, T., and M. King, 1990: Determination of the optical thickness and effective particle radius of clouds from reflected solar radiation measurements. Part I: Theory. *J. Atmos. Sci.*, **47**, 1878–1893, doi:[10.1175/1520-0469\(1990\)047<1878:DOTOTA>2.0.CO;2](https://doi.org/10.1175/1520-0469(1990)047<1878:DOTOTA>2.0.CO;2).
- Platnick, S., 2000: Vertical photon transport in cloud remote sensing problems. *J. Geophys. Res.*, **105**, 22 919–22 935, doi:[10.1029/2000JD900333](https://doi.org/10.1029/2000JD900333).
- Reynolds, D. W., 1980: Observations of damaging hailstorms from geosynchronous satellite digital data. *Mon. Wea. Rev.*, **108**, 337–348, doi:[10.1175/1520-0493\(1980\)108<0337:OODHFG>2.0.CO;2](https://doi.org/10.1175/1520-0493(1980)108<0337:OODHFG>2.0.CO;2).
- Roberts, R., and S. Rutledge, 2003: Nowcasting storm initiation and growth using GOES-8 and WSR-88D data. *Wea. Forecasting*, **18**, 562–584, doi:[10.1175/1520-0434\(2003\)018<0562:NSIAGU>2.0.CO;2](https://doi.org/10.1175/1520-0434(2003)018<0562:NSIAGU>2.0.CO;2).
- Roebeling, R. A., A. J. Feijt, and P. Stammes, 2006: Cloud property retrievals for climate monitoring: Implications of differences between Spinning Enhanced Visible and Infrared Imager (SEVIRI) on *METEOSAT-8* and Advanced Very High Resolution Radiometer (AVHRR) on *NOAA-17*. *J. Geophys. Res.*, **111**, D20120, doi:[10.1029/2005JD006990](https://doi.org/10.1029/2005JD006990).
- Rosenfeld, D., and I. M. Lensky, 1998: Satellite-based insights into precipitation formation processes in continental and maritime convective clouds. *Bull. Amer. Meteor. Soc.*, **79**, 2457–2476, doi:[10.1175/1520-0477\(1998\)079<2457:SBIIPF>2.0.CO;2](https://doi.org/10.1175/1520-0477(1998)079<2457:SBIIPF>2.0.CO;2).
- , U. Lohmann, G. B. Raga, C. D. O'Dowd, M. Kulmala, S. Fuzzi, A. Reissell, and M. O. Andreae, 2008a: Flood or drought: How do aerosols affect precipitation? *Science*, **321**, 1309–1313, doi:[10.1126/science.1160606](https://doi.org/10.1126/science.1160606).
- , W. L. Woodley, A. Lerner, G. Kelman, and D. T. Lindsey, 2008b: Satellite detection of severe convective storms by their retrieved vertical profiles of cloud particle effective radius and thermodynamic phase. *J. Geophys. Res.*, **113**, D04208, doi:[10.1029/2007JD008600](https://doi.org/10.1029/2007JD008600).
- Rossow, W. B., and R. A. Schiffer, 1999: Advances in understanding clouds from ISCCP. *Bull. Amer. Meteor. Soc.*, **80**, 2261–2287, doi:[10.1175/1520-0477\(1999\)080<2261:AIUCFI>2.0.CO;2](https://doi.org/10.1175/1520-0477(1999)080<2261:AIUCFI>2.0.CO;2).
- Schmetz, J., P. Pili, S. Tjemkes, D. Just, J. Kerkmann, S. Rota, and A. Ratier, 2002: An introduction to Meteosat Second Generation (MSG). *Bull. Amer. Meteor. Soc.*, **83**, 977–992, doi:[10.1175/1520-0477\(2002\)083<0977:AITMSG>2.3.CO;2](https://doi.org/10.1175/1520-0477(2002)083<0977:AITMSG>2.3.CO;2).
- Senf, F., F. Dietzsch, A. Hnerbein, and H. Deneke, 2015: Characterization of initiation and growth of selected severe convective storms over central Europe with MSG-SEVIRI. *J. Appl. Meteor. Climatol.*, **54**, 207–224, doi:[10.1175/JAMC-D-14-0144.1](https://doi.org/10.1175/JAMC-D-14-0144.1).
- Sieglaff, J. M., L. M. Cronce, W. F. Feltz, K. M. Bedka, M. J. Pavolonis, and A. K. Heidinger, 2011: Nowcasting convective storm initiation using satellite-based box-averaged cloud-top cooling and cloud-type trends. *J. Appl. Meteor. Climatol.*, **50**, 110–126, doi:[10.1175/2010JAMC2496.1](https://doi.org/10.1175/2010JAMC2496.1).
- , —, and —, 2014: Improving satellite-based convective cloud growth monitoring with visible optical depth retrievals. *J. Appl. Meteor. Climatol.*, **53**, 506–520, doi:[10.1175/JAMC-D-13-0139.1](https://doi.org/10.1175/JAMC-D-13-0139.1).
- Siewert, C. W., M. Koenig, and J. R. Mecikalski, 2010: Application of Meteosat Second Generation data towards improving the nowcasting of convective initiation. *Meteor. Appl.*, **17**, 442–451, doi:[10.1002/met.176](https://doi.org/10.1002/met.176).
- Vallis, G. K., 2006: *Atmospheric and Oceanic Fluid Dynamics: Fundamentals and Large-Scale Circulation*. Cambridge University Press, 769 pp.
- von Storch, H., and F. W. Zwiers, 2002: *Statistical Analysis in Climate Research*. Cambridge University Press, 496 pp.
- Walker, J. R., W. M. MacKenzie Jr., J. R. Mecikalski, and C. P. Jewett, 2012: An enhanced geostationary satellite-based convective initiation algorithm for 0–2-h nowcasting with object tracking. *J. Appl. Meteor. Climatol.*, **51**, 1931–1949, doi:[10.1175/JAMC-D-11-0246.1](https://doi.org/10.1175/JAMC-D-11-0246.1).
- Wapler, K., and P. James, 2015: Thunderstorm occurrence and characteristics in central Europe under different synoptic conditions. *Atmos. Res.*, **158–159**, 231–244, doi:[10.1016/j.atmosres.2014.07.011](https://doi.org/10.1016/j.atmosres.2014.07.011).
- , F. Harnisch, T. Pardowitz, and F. Senf, 2015: Characterisation and predictability of a strong and a weak forcing severe convective event—A multi-data approach. *Meteor. Z.*, **24**, 393–410, doi:[10.1127/metz/2015/0625](https://doi.org/10.1127/metz/2015/0625).
- Wendisch, M., and Coauthors, 2016: ACRIDICON-CHUVA campaign: Studying tropical deep convective clouds and precipitation over Amazonia using the new German research aircraft HALO. *Bull. Amer. Meteor. Soc.*, **97**, 1885–1908, doi:[10.1175/BAMS-D-14-00255.1](https://doi.org/10.1175/BAMS-D-14-00255.1).
- Wilson, J. W., N. A. Crook, C. K. Mueller, J. Sun, and M. Dixon, 1998: Nowcasting thunderstorms: A status report. *Bull. Amer. Meteor. Soc.*, **79**, 2079–2099, doi:[10.1175/1520-0477\(1998\)079<2079:NTASR>2.0.CO;2](https://doi.org/10.1175/1520-0477(1998)079<2079:NTASR>2.0.CO;2).
- Wolters, E. L. A., H. M. Deneke, B. J. J. M. van den Hurk, J. F. Meirink, and R. A. Roebeling, 2010: Broken and inhomogeneous cloud impact on satellite cloud particle effective radius and cloud-phase retrievals. *J. Geophys. Res.*, **115**, D10214, doi:[10.1029/2009JD012205](https://doi.org/10.1029/2009JD012205).
- Zinner, T., H. Mannstein, and A. Tafferner, 2008: Cb-TRAM: Tracking and monitoring severe convection from onset over rapid development to mature phase using multi-channel *Meteosat-8* SEVIRI data. *Meteor. Atmos. Phys.*, **101**, 191–210, doi:[10.1007/s00703-008-0290-y](https://doi.org/10.1007/s00703-008-0290-y).
- Zipser, E. J., 2003: Some views on “hot towers” after 50 years of tropical field programs and two years of TRMM data. *Cloud Systems, Hurricanes, and the Tropical Rainfall Measuring Mission (TRMM)*, Meteor. Monogr., No. 51, Amer. Meteor. Soc., 49–58, doi:[10.1175/0065-9401\(2003\)029<0049:CSVOHT>2.0.CO;2](https://doi.org/10.1175/0065-9401(2003)029<0049:CSVOHT>2.0.CO;2).